PHYSICAL REVIEW LETTERS

Magnetic-Field Generation and Amplification in an Expanding Plasma

K. M. Schoeffler,[1] N. F. Loureiro,[1] R. A. Fonseca,[1,2] and L. O. Silva[1]

[1]*Instituto de Plasmas e Fusão Nuclear—Laboratório Associado, Instituto Superior Técnico,
Universidade de Lisboa, 1049-001 Lisboa, Portugal*
[2]*DCTI/ISCTE—Instituto Universitário de Lisboa, 1649-026 Lisboa, Portugal*

Particle-in-cell simulations are used to investigate the formation of magnetic fields **B** in plasmas with perpendicular electron density and temperature gradients. For system sizes L comparable to the ion skin depth d_i, it is shown that $B \sim d_i/L$, consistent with the Biermann battery effect. However, for large L/d_i, it is found that the Weibel instability (due to electron temperature anisotropy) supersedes the Biermann battery as the main producer of B. The Weibel-produced fields saturate at a finite amplitude (plasma $\beta \approx 100$), independent of L. The magnetic energy spectra below the electron Larmor radius scale are well fitted by the power law with slope $-16/3$, as predicted by Schekochihin *et al.* [Astrophys. J. Suppl. Ser. **182**, 310 (2009)].

Introduction.—The origin and amplification of magnetic fields are central problems in astrophysics [1]. The turbulent dynamo [2,3] is generally thought to be the basic process behind the amplification of a magnetic seed field; however, some other process is required to originate the seed itself. Among the few mechanisms able to do so is the Biermann battery effect, due to perpendicular electron density and temperature gradients [4]. It is often conjectured that the observed magnetic fields in the Universe may be of Biermann origin, subsequently amplified via dynamo action [1]. However, simple theoretical estimates suggest that Biermann-generated magnetic fields **B** should be such that [5–7]

$$\beta \equiv 8\pi P/B^2 \sim (d_i/L)^{-2}, \qquad (1)$$

where P is the plasma pressure, $d_i = c/\omega_{pi}$ is the ion inertial length (with c the speed of light and ω_{pi} the ion plasma frequency), and L is the characteristic length scale of the system. Given the extremely small values of d_i/L typical of astrophysical systems, it is an open question whether such seeds are sufficiently large to account for the microgauss fields observed today.

Megagauss magnetic fields are observed to form in intense laser-solid interaction laboratory experiments [8–12]. In these experiments, the laser generates an expanding bubble of plasma by ionizing a foil of metal or plastic. The plasma is denser closer to the plane of the target foil and hotter closer to the laser beam axis. Perpendicular density and temperature gradients are thus generated, giving rise to magnetic fields via the Biermann effect. Besides their intrinsic interest, these experiments offer a unique opportunity to illuminate a fascinating, and poorly understood, astrophysical process.

In this Letter, we perform *ab initio* numerical investigations of the generation and growth of magnetic fields in a configuration akin to that of laser-generated plasma systems. For small to moderate values of the parameter L/d_i, our simulations confirm the theoretical predictions of Haines [7]; in particular, for $L/d_i \gtrsim 1$, the magnetic fields obey the scaling of Eq. (1). However, when $L/d_i \gg 1$, we find that the plasma is unstable to the Weibel instability [13], which amplifies the magnetic fields such that $\beta \approx 100$, independent of L. These results have strong implications for the interpretation of laser-solid interaction experiments; they also shed new light on the currently accepted view of the origin of the observed cosmic magnetic fields.

Computational model.—We perform a set of particle-in-cell simulations using the OSIRIS framework [14,15]. The initial fluid velocity, electric field, and magnetic field are all uniformly 0. We start with a spheroid distribution of density that has a shorter length scale in one direction: $n = (n_0 - n_b) \cos(\pi R_1/2L_T) + n_b$, if $R_1 < L_T$, n_b; otherwise, $R_1 = \sqrt{x^2 + (L_T/L_n y)^2 + z^2}$ and $n_b = 0.1n_0$ is the uniform background density. The characteristic lengths of the temperature and density gradients generated by the laser beam are denoted by L_T and L_n, respectively. To represent the recently ionized foil, which is flatter in the direction of the laser y, we set $L_T/L_n = 2$. (This is a generic choice that appears to be qualitatively consistent with experiments, e.g., Refs. [9–12]; note, however, that the specific value of L_T/L_n depends on target and laser properties.) The initial velocity distributions are Maxwellian, with a uniform ion thermal velocity v_{Ti0}. The spatial profile for the electron thermal velocity is cylindrically symmetric along the y direction, where it is hottest in the center: $v_{Te} = (v_{Te0} - v_{Teb}) \cos(\pi R_2/2L_T) + v_{Teb}$, if $R_2 < L_T$, v_{Teb}; otherwise, $R_2 = \sqrt{x^2 + z^2}$, resulting in a maximum initial electron pressure $P_{e0} = m_e n_0 v_{Te0}^2/2$. The numerical values of the thermal velocities are $v_{Te0} = 0.2c$ and $v_{Ti0} = v_{Teb} = 0.01c$. Note that in our setup, the pressure

is dominated by the electrons, and thus $\beta \approx \beta_e \equiv 8\pi P_e / B^2$. For simplicity, the boundaries are periodic, but the box is large enough that they do not interfere with the dynamics $[L_{(x,y,z)\,\mathrm{max}} = -L_{(x,y,z)\,\mathrm{min}} = 15/8 L_T]$. In order to investigate a larger range of L_T/d_i, the simulations are run with a reduced mass ratio of 25. The spatial resolution is 16 grid points$/d_e$, or 2.26 grid points$/\lambda_d$, where $d_e = c/\omega_{pe}$ is the electron inertial length (ω_{pe} is the electron plasma frequency) and λ_d is the electron Debye length. The time resolution is $\Delta t \omega_{pe} = 0.07$. The 2D simulations have 196 or 64 particles per cell (ppc); the 3D simulation has 27 ppc.

Biermann regime.—Figure 1 shows contours of constant magnetic energy density and magnetic-field lines from a 3D simulation with $L_T/d_e = 50$ taken at $t\omega_{pe} = 235.2$, after the magnetic-field strength saturates (see Fig. 3). As expected based on the initial conditions, we observe the formation of large-scale azimuthal Biermann magnetic fields which are nearly axisymmetric. Although Biermann generation of magnetic fields has been investigated before [16], this is the first fully self-consistent kinetic 3D simulation.

The axisymmetry in the 3D simulation suggests that a scaling study in system size can be performed using a more computationally efficient 2D setup. To this end, we take a cut of the 3D system at $z = 0$, where the azimuthal (out-of-plane) magnetic fields are in the z direction, and perform a set of 2D simulations with $L_T/d_e = (4, 8, 16, 25, 32, 50, 64, 128, 200, 400)$. For $4 \le L_T/d_e \le 128$, we use 196 ppc. For $L_T/d_e = 200, 400$, we use 64 ppc instead due to computing time limitations; convergence studies at lower values of L_T/d_e do not show significant differences between 196 and 64 ppc. A snapshot taken at the same time of a 2D version of the simulation presented
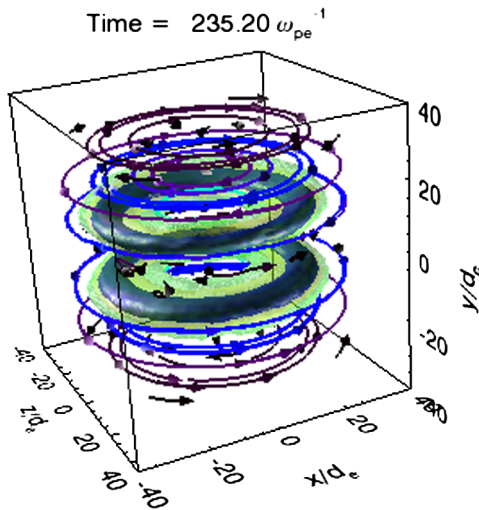
in Fig. 1 is shown in Fig. 2(a) for comparison. The same large-scale magnetic-field structure is manifest, with very similar levels of B_z.

The time trace of the maximum magnetic-field strength for a selection of cases can be seen in Fig. 3(a). For small systems $L_T/d_e < 50$, the magnetic field reaches a maximum and then decays away. On the other hand, we observe that for $L_T/d_e > 50$, the magnetic field saturates at around its peak value.

Figure 3(b) shows the scaling with system size of the maximum and the average magnitude of the magnetic field (the square root of B_z^2 averaged in a box $2L_T \times 2L_n$ surrounding the expanding bubble) at the time when the field saturates (or peaks for $L_T/d_e < 50$). There are three distinct regions in this plot. For $L_T/d_e < 25$ (i.e., $L_T/d_i \lesssim 5$), the magnetic field increases with system size. This stage is followed by a region where the saturated amplitude of the field decreases as d_i/L_T, which lasts while $L_T/d_e < 100$. These two stages confirm the theoretical prediction of Haines [7]: in very small systems, there is a competition between the Biermann battery effect and microinstabilities (the ion acoustic and the lower hybrid drift instabilities), triggered by an electron drift velocity in excess of the ion acoustic speed, which suppress the
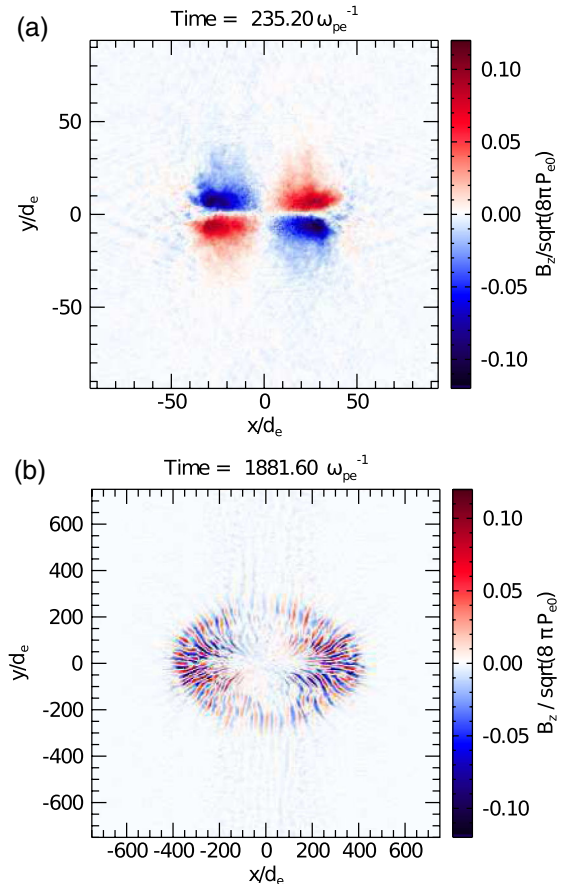

FIG. 1 (color online).　Magnetic energy contours after saturation ($t\omega_{pe} = 235.2$; see Fig. 3) from a 3D simulation with $L_T/d_e = 50$. Lighter to darker colors represent $B^2/8\pi P_{e0} = 0.0035, 0.0071, 0.0106$. Several magnetic-field lines are also displayed.

FIG. 2 (color online).　Out-of-plane magnetic field B_z after saturation (see Fig. 3) for (a) $L_T/d_e = 50$ and (b) $L_T/d_e = 400$.
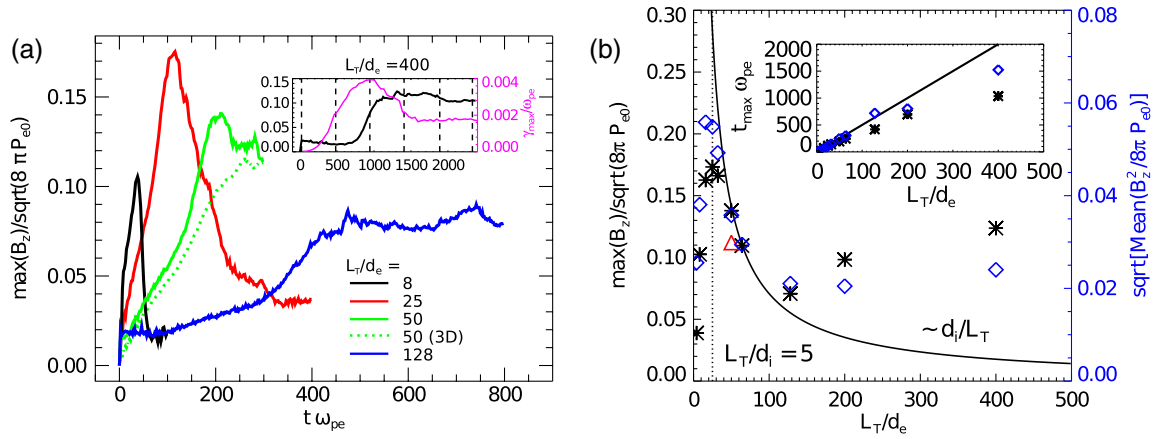
FIG. 3 (color online).   (a) Maximum B_z vs time for a selection of system sizes (L_T/d_e). The inset shows the $L_T/d_e = 400$ case (black line). The magenta line is the maximum Weibel growth rate $\gamma_{\max}$ at $y = 0$. Dashed lines identify the times at which the spectra of Fig. 5 are calculated. (b) Maximum (asterisks) and average (diamonds) magnitudes of B_z vs L_T/d_e. The triangle represents the maximum B_z for the 3D run. The solid curve is $\max(B_z)/\sqrt{8\pi P_{e0}} = \sqrt{2}d_i/L_T$; the dotted line indicates $L_T/d_i = 5$. The inset shows the time to maximum magnetic field $t_{\max}$ vs L_T/d_e. The solid line indicates $t_{\max} = L_T/v_{Te0}$.

Biermann fields. As the system becomes larger, the electron drift velocity decreases. (Larger systems have larger-scale magnetic fields, and therefore lower currents.) The micro-instabilities thus become progressively less virulent until their complete suppression, whereupon we encounter a "pure" Biermann regime, as described in Eq. (1). Inspection of the simulations for $L_T/d_e < 50$ at times after the magnetic field reaches its peak value shows clear electric-field perturbations along $y = 0$, consistent with the ion acoustic instability. These are exemplified for $L_T/d_e = 25$ in Fig. 4. Note that the density gradient goes to 0 at $y = 0$, ruling out the lower hybrid drift instability as the cause of the decay of the magnetic field.

Weibel regime.—An unexpected third regime is encountered for $L_T/d_e > 100$. In that region of Fig. 3(b), the magnetic field produced in our simulations no longer follows the predicted d_i/L_T Biermann scaling, but rather increases with the system size and appears to tend to a constant, finite value $\beta_e \approx 100$.

In this new regime, the magnetic fields are produced by the Weibel instability [13]. The initial cloud of plasma expands due to the imposed density gradient, generating both outward ion and hot electron flows. The velocities of the electron flows vary along the temperature gradient. The higher temperature flows originating in the center stream past lower temperature inward flows originating further outward, which maintains quasineutrality. This generates a larger velocity spread (larger temperature) in the direction of the flow, while the perpendicular temperature remains unaffected. It is this temperature anisotropy that drives the Weibel instability [13]. Note that along $x = 0$, where the temperature gradient is 0, no anisotropy is generated, and thus the Weibel instability is not observed [see Fig. 2(b)].

As exemplified in Fig. 2(b) for our largest simulation ($L_T/d_e = 400$), the large-scale coherent Biermann magnetic

fields characteristic of the smaller systems are replaced by nonpropagating magnetic structures with very large wave numbers ($kd_e \sim 0.2$) and with a transverse wave vector **k** perpendicular to the direction with a larger temperature. These features are consistent with the Weibel instability [13,17,18]. In addition, we have compared our results with the analytic growth rate predicted by Weibel [13]. In our simulations, we observe an enhanced temperature in the direction of the density gradient (parallel) as high as $A \equiv T_{\|e}/T_{\perp e} - 1 \approx 2.0$. In a cut at $y = 0$, we calculate the Weibel growth rate γ for the fastest growing k ($k_{\max}$) using the locally measured values of n, $T_{\perp e}$, and A. The maximum γ of this cut $\gamma_{\max}$ is plotted vs time in Fig. 3(a), showing a peak when the magnetic-field strength rises exponentially and a subsequent drop corresponding to the loss of anisotropy after saturation. The magnitude of the growth rate thus calculated is also consistent within a factor of 2, with $k_{\max}d_e \approx 0.2$, analogous to the structures in Fig. 2(b).

The transition between the Biermann and Weibel regimes is also visible in the inset of Fig. 3(b), where we show the time to reach the maximum magnetic field $t_{\max}$ as a function of system size. For $L_T/d_e < 50$, we find that
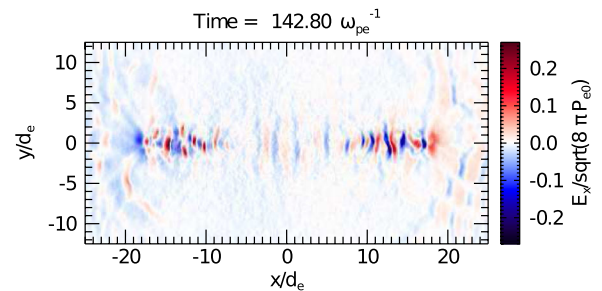

FIG. 4 (color online).   Electric field in the x direction E_x for $L_T/d_e = 25$ at $t\omega_{pe} = 142.8$.

$t_{max} \sim L_T/v_{Te0}$. A linear in time scaling is indeed to be expected for Biermann-generated fields; also, at these small scales, the electrons are not coupled to the ions and are thus free to move at their thermal velocity. A transition to a logarithmic dependence on the system size occurs after $L_T/d_e > 50$; this is expected since the Weibel instability amplifies the magnetic fields at an exponential rate. Note that the Weibel instability cannot occur below a certain system size because it is suppressed by the strong, large-scale Biermann fields. (We have confirmed this suppression numerically by running a similar setup where the Biermann effect is not present; see also Ref. [19].)

We have performed additional studies that confirm our conclusions up to a mass ratio of $m_i/m_e = 2000$, at which point the results have converged. With these more realistic mass ratios, the saturated magnetic field increases less than twice the value obtained for $m_i/m_e = 25$. These results will be presented elsewhere.

Spectra.—Figure 5(a) shows the spectrum of B_z^2 for our largest simulation ($L_T/d_e = 400$) at the times indicated in the inset of Fig. 3(a). At early times, a peak rapidly forms at $kd_e \approx 0.01$, which corresponds to the large-scale Biermann-generated magnetic field. At later times, a second peak corresponding to the Weibel-generated magnetic fields begins to form at $kd_e \approx 0.2$ and eventually saturates at $kd_e \approx 0.1$; this scale corresponds to $k\rho_e = 1$, where ρ_e is the electron Larmor radius based on the maximum B_z at saturation. Therefore, the Weibel-generated fields saturate when $\beta_e = (\rho_e/d_e)^2 \approx 100$ (cf. Refs. [17,20]), independently of the system size, as shown in Fig. 3(b).

Another remarkable feature yielded by the spectra of Fig. 5 is the power law behavior of the magnetic energy at sub-ρ_e scales, with a slope close to $-16/3$. A less steep power law appears to exist at smaller scales, but this is not present in the 3D simulation, as seen in Fig. 5(b). Note that this slope occurs for both small and large systems and is not, therefore, a consequence of the Weibel instability. Such a power law dependence was theoretically predicted using gyrokinetic theory in Ref. [21], where it was identified as resulting from an entropy cascade of the electron distribution function at scales below $k\rho_e \sim 1$. We believe this is the first 3D confirmation of that prediction, although similar observations have been made in 2D simulations [22].

Conclusions.—We have performed fully kinetic simulations of magnetic-field generation and amplification in expanding, collisionless plasmas with perpendicular density and temperature gradients. For relatively small systems $L_T/d_e < 100$, we observe the production of large-scale magnetic fields via the Biermann battery effect, fully confirming the theoretical predictions of Haines [7], in particular, the scaling of the magnetic-field strength with d_i/L_T. For larger systems, however, we discover a new regime of magnetic-field generation: the expanding plasmas are Weibel unstable, giving rise to small-scale ($kd_e \sim 0.2$) magnetic fields whose saturated amplitude is
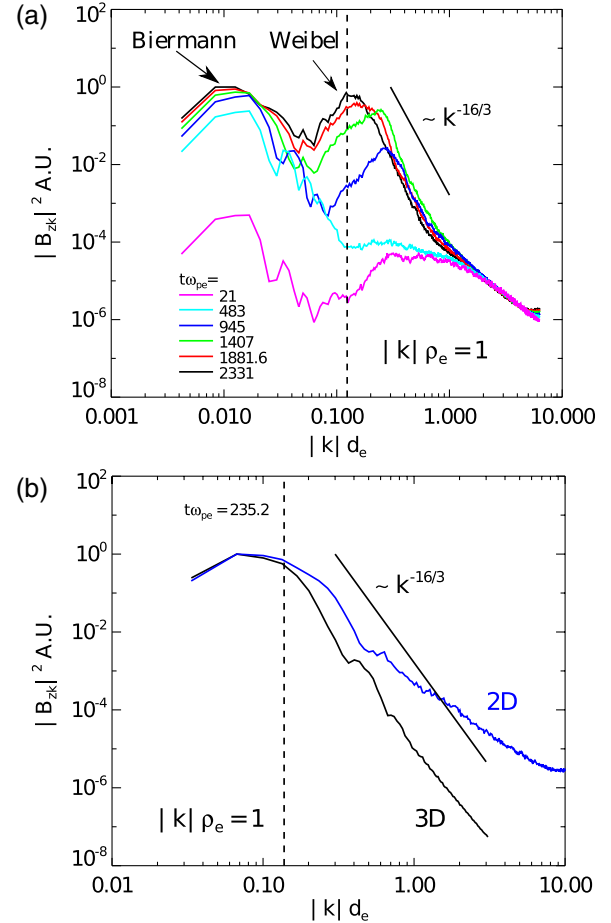

FIG. 5 (color online). Fourier spectrum of B_z^2 for (a) $L_T/d_e = 400$ and (b) $L_T/d_e = 50$. In (a), the spectrum is shown at several different times [see Fig. 3(a)], while in (b), the 3D (black curve) and the 2D (blue curve) simulations are shown for $t\omega_{pe} = 235.2$. The dashed lines represent where $k\rho_e = 1$, based on the maximum magnetic field. The solid black lines indicate a power law of $k^{-16/3}$.

such that $\beta_e \approx 100$, independent of system size, and thus much larger than would be predicted for such systems on the basis of the Biermann mechanism. We note that both of these regimes can, in principle, be probed by existing experiments. For example, the $L_T/d_i \approx 1$ regime (Biermann) is accessible to the Vulcan laser [9], whereas $L_T/d_i \approx 100$ (Weibel) is reachable by an OMEGA laser [10]. In practice, however, collision frequencies that are large compared to the electron transit time prohibit electron temperature anisotropies, thereby inhibiting the Weibel instability. If less collisional regimes can be attained in the experiments, it may be possible to experimentally investigate the transition from Biermann- to Weibel-produced magnetic fields that we have uncovered here.

In the context of (largely collisionless) astrophysical plasmas, our results may significantly impact the canonical picture of cosmic magnetic-field generation [1], by suggesting that Biermann seed fields may be preamplified

exponentially fast via the Weibel instability up to reasonably large values (i.e., independent of the system size) previous to turbulent dynamo action.

[1] R. M. Kulsrud and E. G. Zweibel, Rep. Prog. Phys. **71**, 046901 (2008).

[2] R. M. Kulsrud and S. W. Anderson, Astrophys. J. **396**, 606 (1992).

[3] A. Brandenburg, D. Sokoloff, and K. Subramanian, Space Sci. Rev. **169**, 123 (2012).

[4] L. Biermann, Z. Naturforsch. **5a**, 65 (1950).

[5] C. E. Max, W. M. Manheimer, and J. J. Thomson, Phys. Fluids **21**, 128 (1978).

[6] R. S. Craxton and M. G. Haines, Plasma Phys. **20**, 487 (1978).

[7] M. G. Haines, Phys. Rev. Lett. **78**, 254 (1997).

[8] J. A. Stamper, K. Papadopoulos, R. N. Sudan, S. O. Dean, and E. A. McLean, Phys. Rev. Lett. **26**, 1012 (1971).

[9] P. M. Nilson, L. Willingale, M. C. Kaluza, C. Kamperidis, S. Minardi, M. S. Wei, P. Fernandes, M. Notley, S. Bandyopadhyay, M. Sherlock *et al.*, Phys. Rev. Lett. **97**, 255001 (2006).

[10] C. K. Li, F. H. Séguin, J. A. Frenje, J. R. Rygg, R. D. Petrasso, R. P. J. Town, P. A. Amendt, S. P. Hatchett, O. L. Landen, A. J. Mackinnon *et al.*, Phys. Rev. Lett. **97**, 135003 (2006).

[11] C. K. Li, F. H. Seguin, J. A. Frenje, J. R. Rygg, R. D. Petrasso, R. P. J. Town, O. L. Landen, J. P. Knauer, and V. A. Smalyuk, Phys. Rev. Lett. **99**, 055001 (2007).

[12] N. L. Kugland, D. D. Ryutov, P.-Y. Chang, R. P. Drake, G. Fiksel, D. H. Froula, S. H. Glenzer, G. Gregori, M. Grosskopf, M. Koenig *et al.*, Nat. Phys. **8**, 809 (2012).

[13] E. S. Weibel, Phys. Rev. Lett. **2**, 83 (1959).

[14] R. A. Fonseca, L. O. Silva, F. S. Tsung, V. K. Decyk, W. Lu, C. Ren, W. B. Mori, S. Deng, S. Lee, T. Katsouleas, and J. C. Adam, Lect. Notes Comput. Sci. **2331**, 342 (2002).

[15] R. A. Fonseca, S. F. Martins, L. O. Silva, J. W. Tonge, F. S. Tsung, and W. B. Mori, Plasma Phys. Controlled Fusion **50**, 124034 (2008).

[16] A. Thomas, M. Tzoufras, A. Robinson, R. Kingham, C. Ridgers, M. Sherlock, and A. Bell, J. Comput. Phys. **231**, 1051 (2012).

[17] F. Califano, F. Pegoraro, S. V. Bulanov, and A. Mangeney, Phys. Rev. E **57**, 7048 (1998).

[18] R. A. Fonseca, L. O. Silva, J. W. Tonge, W. B. Mori, and J. M. Dawson, Phys. Plasmas **10**, 1979 (2003).

[19] K. Molvig, Phys. Rev. Lett. **35**, 1504 (1975).

[20] D. V. Romanov, V. Y. Bychenkov, W. Rozmus, C. E. Capjack, and R. Fedosejevs, Phys. Rev. Lett. **93**, 215004 (2004).

[21] A. A. Schekochihin, S. C. Cowley, W. Dorland, G. W. Hammett, G. G. Howes, E. Quataert, and T. Tatsuno, Astrophys. J. Suppl. Ser. **182**, 310 (2009).

[22] E. Camporeale and D. Burgess, Astrophys. J. **730**, 114 (2011).